Modeling the transport of water and ionic tracers in a micrometric clay sample

Pauline Bacle [a,], Jean-François Dufrêche [b], Benjamin Rotenberg [a], Ian C. Bourg [c], Virginie Marry [a]

[a] Sorbonne Universités, UPMC Univ. Paris 06, CNRS, Laboratoire PHENIX, Case 51, 4 place Jussieu, F-75005 Paris, France
[b] CEA, CNRS, Université Montpellier, UMR 5257 ICSM, F-34000 Montpellier, France
[c] Civil and Environmental Engineering and Princeton Environmental Institute, Princeton University, Princeton, NJ 08544, USA

a b s t r a c t

Brownian dynamics simulations were performed to examine the self-diffusion of cationic (Na^+), anionic (Cl^-), and water tracers in a saturated compacted clay at the micrometric scale. Clay minerals particles, representing stacks of montmorillonite layers, are modeled as cylindrical platelets with characteristics that depend on the dry bulk density of the porous medium, ρ_b. The tracers are allowed to diffuse between the platelets with their diffusion coefficient in bulk aqueous solution as well as inside the platelets with a diffusion coefficient that depends on the hydration level of the interlayer pores as determined from experiments or molecular dynamics simulations. The probability for a tracer to enter a platelet is related to its charge as predicted by the Poisson–Boltzmann equation. The apparent diffusion coefficients are calculated as a function of ρ_b for various salinities and compared with the values obtained from tracer diffusion experiments available in the literature. Despite the simplicity of the clay model, the simulations predict most features of the experimental data and keep the door open for further improvements.

Keywords:
Diffusion
Brownian dynamics
Montmorillonite
Modeling
Molecular dynamics

1. Introduction

Clay minerals are highly abundant natural materials that play significant roles in many environmental and engineering applications because of their high cation exchange capacity and specific surface area, swelling behavior, water and solute retention properties, and low permeability. In particular, compacted swelling clay minerals (smectites) has been proposed as barrier materials for the long-term isolation of high-level radioactive waste in geologic formations (McCombie, 1997; H12 report, 2000; ANDRA report, 2001). Because of the very low hydraulic permeability of compacted clay, molecular diffusion is the predominant mass transfer process in these barriers. This has motivated numerous experimental and theoretical studies of diffusion in compacted, water-saturated smectite, as well as in smectite-rich materials commonly known as bentonite. A particularly large experimental database exists for the self-diffusion of cations (Cs^+, Sr^{2+}, Na^+) (Kozaki et al., 1996a, 1996b, 1998a; Liu et al., 2003a), anions (I^-, Cl^-, TcO_4^-) (Sato et al., 1992; Kozaki et al., 2001a) and water tracers such as HDO or HTO (Nakazawa et al., 1999; Nakashima, 2001; Sato and Suzuki, 2003; Suzuki et al., 2004) in clayey media at various degrees of compaction with dry bulk densities from $\rho_b = 0.02$ to 1.95 kg L^{-1}, where ρ_b is the ratio of the mass of solid to the volume of the sample, i.e., $\rho_b = m_{clay}/V_{TOT}$.

The transport of solutes in clays can be quantified by empirical parameters such as adsorption constants or effective diffusion coefficients, which are measured at the macroscopic scale but need to be related to microscopic mechanisms. One difficulty arises from the complex, multi-scale structure of clay materials. Clay mineral particles consist of stacks of parallel negatively-charged layers separated by interlayer nanopores. Consequently, compacted smectite contains two major classes of pores: interlayer nanopores (located inside the particles) and larger mesopores (located between the particles). The permanent negative charge of the clay mineral layers is compensated by counterions located both in the interlayer nanopores and on the external surfaces of particles. Both types of cations are mobile and contribute to the overall cation diffusive flux (Glaus et al., 2007; Melkior et al., 2009). In contrast, inert anions such as Cl^- can be viewed as non-adsorbing species that migrate in the 'free' pore water (far from the clay mineral surfaces) and, to some extent, in the electric double layer water on the external surfaces of particles. The partial exclusion of anions from the interlayer space due to the negative layer charge has been extensively studied by molecular dynamics simulations (Rotenberg et al., 2007; Hedström and Karnland, 2012) and experimental methods (Kozaki et al., 2001a; Van Loon et al., 2007) and modeled using mean-field theories such as the mean electrostatic model and the Poisson-Boltzmann equation (Birgersson and Karnland, 2009; Jardat et al., 2009).

Along with experiments, conceptual models have been developed to describe the transport of water and solutes in water-saturated bentonite Bourg et al. (2006); Bourg and Sposito (2010) and simulations from

Corresponding author.
E-mail address: pauline.bacle@upmc.fr (P. Bacle).

the atomic scale (Delville, 1992; Leote de Carvalho and Skipper, 2001; Skipper et al., 2006) to larger scales (Churakov and Gimmi, 2011; Churakov et al., 2014) have been performed. In particular, an emerging concept consists in explicitly accounting for nanopores (nanometer-scale interlayer pores) and mesopores (all other pores) as two distinct compartments of the bentonite pore space (Hueckel et al., 2002; Bourg et al., 2006).

In this paper, the diffusion of water, Na^+ and Cl^- in compacted, water-saturated bentonite was studied at the micrometric scale using Brownian dynamics (BD) simulations. The clay mineral particles are modeled as cylindrical platelets, the dimensions and the distribution of which depend on ρ_b. The description of the platelets based on experimental data is made in Section 2.1. The principles of the procedure for generating clay samples are described in Section 2.2. Brownian dynamics simulations are, then, carried out according to the method described in Section 3.1. Briefly, tracers are modeled as moving through the sample with different diffusion coefficients depending on whether they are located inside or outside a platelet. Diffusion in the interparticle pores (i.e., outside the platelets) occurs with the same diffusion coefficient as in bulk solution, whereas diffusion inside the platelet is slowed down by confinement. In addition, tracer mass fluxes across particle edge boundaries are influenced by salinity and the valence of the tracer. Micrometer-scale diffusion coefficients in the modeled clay sample are calculated from the tracer trajectories obtained from BD simulations. Both the concentrations and the diffusion coefficients in the interlayer and interparticle pores are necessary input parameters for the BD simulations. Section 3.2 describes the evaluation of these parameters based on experimental data and molecular dynamics (MD) simulations. The existing experimental database on centimeter-scale apparent diffusion coefficients in compacted, water-saturated clay is described in Section 4. The features of the samples are discussed in the first part of Section 5, while the accuracy of the interlayer/interparticle pore model is evaluated by comparing predicted diffusion coefficients with the experimental database in the second part of Section 5. Finally, the last section contains a conclusive discussion.

2. Model of clay microstructure

In this model, the sample is composed of a set of clay mineral particles represented as cylindrical platelets overlapping each other. As explained below, the dimensions of the platelets and the volume fraction they occupy in the simulation box are calculated for each dry density ρ_b. These quantities are then used to generate a porous medium at each ρ_b, as represented on Fig. 1.

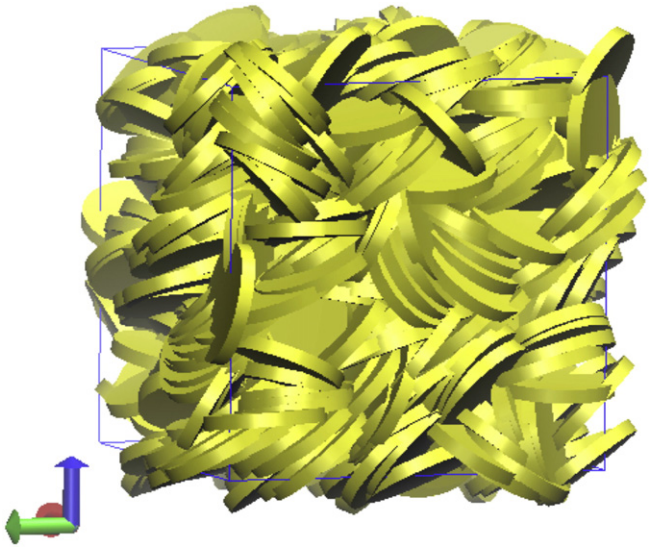

Fig. 1. A Gay–Berne configuration of 1000 platelets in a cubic box of length 19,186 Å corresponding to $\rho_b = 0.7$ kg L^{-1} (parameters: $R = 2500$ Å, $h = 688.3$ Å).

2.1. Dimensions of the platelets

Clay mineral particles consist of tens of negatively-charged stacked aluminosilicate layers, with lateral dimensions of hundreds of nanometers (Arnott, 1965). In the present model, the particles are modeled as cylindrical platelets with a diameter of 500 nm, each consisting of 20 stacked clay mineral layers (see Fig. 2).The parameter ΔL is defined as the distance between the mid-planes of two consecutive clay mineral layers; the height of each platelet is, then, $h = 20 \times \Delta L$. The distance ΔL depends on the dry density of the sample, because smectite interlayer nanopores (and, hence, the clay mineral particles contain a variable amount of water. Two swelling regimes are observed. At first, the process occurs in discrete steps (crystalline swelling) through the formation of crystallographically ordered layers of water molecules between the silicate layers. Beyond three layers of water molecules, the swelling is better described as a continuous phenomenon until isolated aggregates are formed and a colloidal dispersion is obtained. During the transition from the crystalline to osmotic swelling, the value of ΔL jumps from ~18.5 Å to ~40 Å (Norrish, 1954).

Here we consider the case of a montmorillonite (the predominant type of smectite clay mineral) with Na^+ counterions (designated as Na^+ Mt). On the basis of X-ray diffraction (XRD) data reported for Na^+ Mt (Norrish and Quirk, 1954; Calvet, 1973; Fu et al., 1990; Cases et al., 1992; Kozaki et al., 2001a; Ferrage et al., 2005b), the clay is modeled as having stable states at $\Delta L_{dry} = 9.5$ Å (dry clay), $\Delta L_{1W} \sim 12.5$ Å (one layer hydrate, 1W), $\Delta_{L2W} \sim 15.5$ Å (two layer hydrate, 2W) and $\Delta L_{3W} \sim 18.5$ Å (three layer hydrate, 3W) (Bourg and Sposito, 2010; Holmboe et al., 2012). The 3 Å increase in the ΔL between stable swelling states is consistent with the expected thickness of a monolayer of water molecules. Based on the XRD data of Holmboe et al. (2012), the interlayer spaces are viewed as a mixture of 1W and 2W states if $\rho_b \geq 1.7$ kg L^{-1} and as a mixture of 2W and 3W states if ρ_b ranges from 1.35 to 1.7 kg L^{-1}. The average interlayer distance ΔL is then calculated for $\rho_b > 1.35$ kg L^{-1} with the relation:

$$\Delta L_{nW+mW} = x_{nW}\Delta L_{nW} + (1-x_{nW})\Delta L_{mW}. \quad (1)$$

where x_{nW} is the fraction of nW state in the mixture $nW - mW$. In view of the evolution of x_{nW} with ρ_b given in Holmboe et al. (2012), the fraction x_{nW} of nW state in the mixture $nW - mW$ is considered to vary almost linearly between the boundaries of this domain: for instance, x_{3W} varies linearly from 0 to 1 as ρ_b varies from 1.7 to 1.35 kg L^{-1}. On the basis of this assumption and Eq. (1), ΔL_{nW+mW} can be evaluated for every $\rho_b > 1.35$ kg L^{-1}. The values are given in Table I of the Supporting information.

Once ΔL is calculated as described above, the fraction of fluid in the interlayer pores f_{il}, defined as the ratio between the volume of interlayer pores, V_{il}, and the volume of all pores, V_p, can be calculated using the following relation (where V_{TOT} is the total volume of the sample, V_{pl} is the volume occupied by the platelets in the sample)

$$f_{il} = \frac{V_{il}}{V_p} = \frac{V_{il}}{V_{il} + V_{TOT} - V_{pl}} = \frac{x_{il}}{x_{il} + 1/\varphi - 1}. \quad (2)$$

On the right side of Eq. (2), x_{il} is the volume fraction of pore space in each platelet and $\varphi = \frac{V_{pl}}{V_{TOT}}$ is the volume fraction of platelets in the entire sample. The value of x_{il} is a simple function of ΔL

$$x_{il} = \frac{\Delta L - \Delta L_{dry}}{\Delta L}. \quad (3)$$

Moreover, the evolution of φ with ρ_b can be determined using

$$\varphi = \frac{V_{pl}}{V_{TOT}} = \frac{\rho_b}{\rho_{pl}}, \quad (4)$$

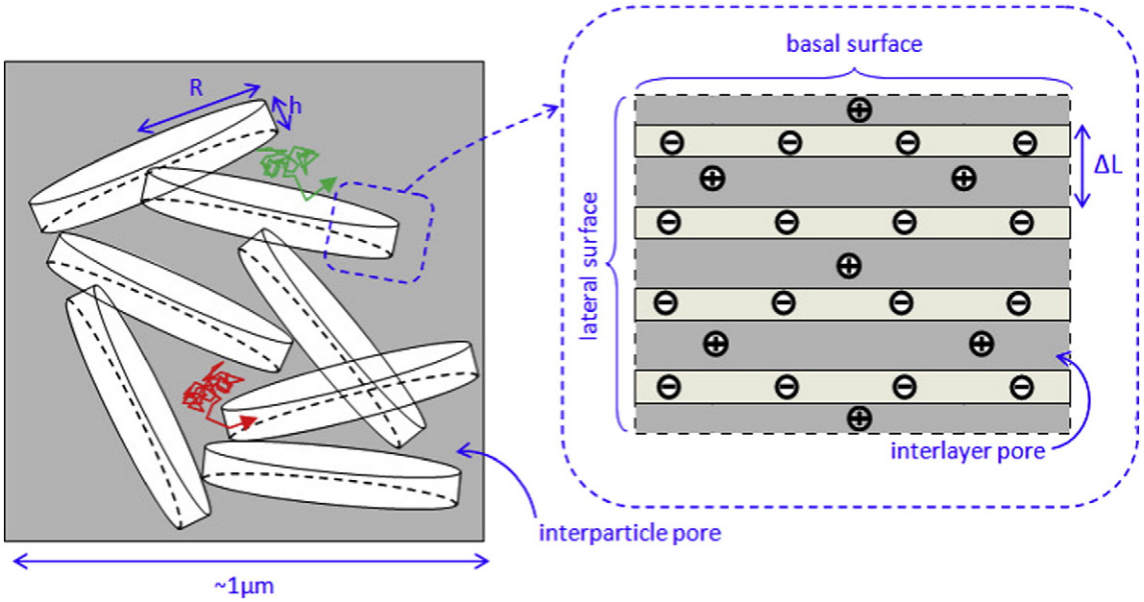

Fig. 2. Schematic illustration of the model. Two trajectories are shown: the green trajectory represents the tracer bouncing back on the basal surface of a platelet, the red one represents the tracer entering a platelet through its lateral surface. The radius R, the height of the platelet h and the interlayer space ΔL are indicated. The dotted box illustrates the structure of a platelet of height $h = 4\Delta L$: The 4 solid layers are colored in light gray while interlayer pores appear in a darker shade.

where $\rho_{pl} = m_{clay}/V_{pl}$, the mass density of the platelet, can be calculated from

$$\rho_{pl} = \frac{M}{N_A \times A \times \Delta L} = \frac{\alpha}{\Delta L}. \tag{5}$$

In Eq. (5), M is the molecular (unit cell) mass of montmorillonite and A is the corresponding surface area. The value of α can be estimated from the accessory mineral inventory of bentonites reported by Karnland et al. (2006) to $\alpha = 26.5$ for ΔL in Å and ρ_{pl} in kg L^{-1}. From the equations presented above, f_{il} is found to increase from $f_{il} = 0.88$ for $\rho_b = 1.35$ kg L^{-1} to $f_{il} = 0.96$ for $\rho_b = 1.8$ kg L^{-1}. Indeed, when the clay is compressed, the interparticle pores are the first to decrease in width while the interlayer pores remain in stable hydration states due to the strong interactions between the cations and the water molecules.

The behavior below $\rho_b = 1.35$ kg L^{-1} is different because the swelling becomes continuous. Here, beyond three layers of water molecules, compaction is reckoned to have the same effect on the size of the pores inside a particle as on the interparticle pores. As a result, f_{il} is assumed to be essentially invariant with ρ_b for densities inferior to 1.35 kg L^{-1} and the value obtained for this limit ($f_{il} = 0.88$) is kept for $\rho_b < 1.35$ kg L^{-1}. Using Eqs. (2)–(5), the value of ΔL is then computed as a function of ρ_b for this range of densities with the relation

$$\Delta L = \Delta L_{dry} + f_{il} \times \left(\frac{\alpha}{\rho_b} - \Delta L_{dry}\right). \tag{6}$$

Let us note that Eq. (6) with fixed $f_{il} = 0.88$ gives $\Delta L = 40$ Å for a density of 0.6 kg L^{-1}, which is consistent with the evolution of ΔL with ρ_b found by Norrish (1954) and supports the assumption made on the evolution of f_{il}.

2.2. Platelets organization

Once the height of the platelets is known for one value of ρ_b, the platelets are arranged in a micrometer-sized box and the volume fraction occupied by the platelets φ is calculated with Eqs. (4) and (5). The values of φ for each ρ_b are given in Table I of the Supporting information.

A sample is generated by introducing the platelets in the simulation box until the fraction φ corresponding to a given density is reached. The platelets are located by the position of their center of mass and the orientation of the vector normal to the platelet. Since models of sedimentation and other models using cylindrical platelets are not able to build highly compacted samples, a two-step approach is used. First, the positions and orientations of the platelets are determined from molecular dynamics simulations using a system inspired by Ebrahimi et al. (2014) consisting of ellipsoidal particles described by Gay–Berne (GB) potentials. This allows to generate a realistic configuration which accounts for the fact that the orientation of a particle is influenced by the surrounding particles. In a second step, the resulting positions and orientations are assigned to cylindrical platelets with the dimensions determined in the previous section. Then, φ can be calculated as the volume occupied by the platelets divided by the volume of the box. When two platelets intersect each other, their common volume is only counted once to evaluate φ. The cylinders are thus given a priority order to define the platelet to which a common volume belongs. Consequently, the first platelet is unaffected while the last one is divided into fragments because it is intersected by many platelets with higher priorities. In this way, the model indirectly takes into account the flexibility of the particles by compensating for the rigidity of the platelets by allowing several platelets with different orientations to overlap. Finally, the final configurations are obtained by doing successive homotheties on the position of the particles and the size of the box while keeping the structural parameters of the platelets fixed until the right fraction φ is reached. For illustrative purposes, Fig. 1 shows a so-called Gay–Berne configuration obtained for $\rho_b = 0.7$ kg L^{-1}. As mentioned above, this method allows to reach higher densities than a sedimentation model would. For instance, structures resulting from the random sequential deposition of non overlapping grains of several sizes and shapes were investigated in a work by Coelho et al. (1997): The particles were dropped one at a time in a gravitational field with a non overlap condition. While those structures demonstrate interesting results regarding the fact that effective transport properties are oblivious to the grain shape, they only account for rigid particles with given orientations and therefore fail to reach high densities. Indeed, numerical simulations

of the sedimentation of cylinders yield solid fractions up to 0.580 at best whereas the two-step method presented in this paper allows to generate samples with φ values up to 0.986. For comparison purposes, simpler but less realistic configurations (called 'random' configurations in this paper) were also computed where the positions of the platelets in the simulation box are chosen randomly with an isotropic distribution of the orientations of the platelets.

One of the main advantages of the present model is certainly its simplicity. However, it can appear rather crude and unrealistic, especially in the light of alternative clay microstructure modeling approaches such as the grain reconstruction procedure developed by Thovert et al. (2001) or the model proposed by Tyagi et al. (2013). The procedure of Thovert et al. (2001) is based only on geometrical parameters measurable from images of real samples and uses polydisperse Poisonian penetrable spheres conditioned by the experimental solid size distribution. However, it only accounts for the microporosity of the medium while, even if they are not explicitly represented, the present model includes the interlayer pores in the evaluation of the thickness of the particles and in the parameters used as input for the Brownian Dynamics simulations (discussed in the next section). As for the approach chosen by Tyagi et al. (2013), it explicitly accounts for both the interlayer pores and the larger inter-grains pores according to the desired hydration state, microporosity and pore size distribution. Moreover, it uses a representative ensemble of grains obtained by a lattice Monte Carlo technique to generate anisotropic structures with grains of different minerals according to the clay composition. It certainly allows for more realistic particles shape but it is not as easy to handle as a collection of cylindrical platelets.

3. Brownian dynamics simulations

Brownian dynamics simulations based on the solution of the diffusion equation were used to study the diffusion of several species (referred to as *tracers*) in the clay sample described in the previous section. For three-dimensional pure diffusion, the concentration profile is given by the following expression (Crank, 1975):

$$C(r,t) = \frac{M}{(4\pi D_a t)^{3/2}} \exp\left(-\frac{r^2}{4D_a t}\right) \tag{7}$$

where D_a is the apparent diffusion coefficient of the tracer in the sample, t is the diffusion time, r is the distance from a uniform source of the species of interest, and M is the total amount of substance diffusing.

3.1. Method

A tracer is placed in the simulation box containing a configuration of platelets. Its initial position is chosen according to the concentrations of the tracer inside and outside the platelets (which will be defined in Section 3.2). At each time step, the 3D displacement of the tracer $\vec{d}$ is chosen from the following Gaussian distribution:

$$p_i = \frac{1}{(4\pi D_i \Delta t)^{3/2}} \exp\left(-\frac{d^2}{4D_i \Delta t}\right), \tag{8}$$

where D_i is the diffusion coefficient in the environment i (i.e., either inside or outside the platelets), Δt is the time step of the simulation, and d is the norm of the displacement vector. This trial move is then accepted or rejected as follows. One the one hand, when the tracer goes from one platelet to another, the displacement is always accepted (i.e., the probability of crossing from one particle to another $p_{acc}^{p\to p}$ is 1). This has an important impact on the way this model describes the porous medium. In fact, although the fragmentation of the platelets is unavoidable due to the overlap between the platelets, the porous medium should not be seen as constituted of very small and numerous clay mineral particles, which would not be realistic. Rather, the fact that $p_{acc}^{p\to p}$ is equal to 1 means that when the tracer goes from one platelet to another, it actually stays in a same clay mineral particle. The change of orientation can be viewed as a consequence of the flexibility of the clay mineral particles.

On the other hand, if the displacement results in an entrance into or an exit from the interplatelet space, it obeys two rules. Firstly, if it goes through the basal surface of a platelet (the surface normal to the orientation vector, see Fig. 2), the tracer bounces back on the surface: The direction of the displacement is reflected on the surface and the tracer travels another distance $d' = d - d_c$ where d_c is the distance already covered by the tracer (i.e., the distance between the origin and the impact point on the surface). Secondly, if it goes through a lateral surface (see Fig. 2), the displacement is either accepted or rejected according to the following probability given by the detailed balance and the Metropolis criteria (Frenkel and Smit, 1996):

$$p_{acc}^{i\to j} = \min\left\{1; \frac{c_j}{c_i} \times \left(\frac{D_i}{D_j}\right)^{3/2} \times \exp\left(-\frac{d^2}{4D_j\Delta t} + \frac{d^2}{4D_i\Delta t}\right)\right\}, \tag{9}$$

where c_i/c_j is the equilibrium ratio of tracer concentrations in environments j and i (either particles (p) or interparticle pores (0)). If the displacement is rejected, the tracer bounces back on the surface.

Several trajectories of 5.10^{10} ps with a time step $\Delta t = 10$ ps were simulated. Trajectories with smaller time steps were simulated and gave similar results. For each trajectory, the mean square displacement (MSD) is calculated as a function of time τ. An estimation of the diffusion coefficient D_a is then obtained from the linear fit of the MSD curve between 0 and 2.10^9 ps according to $\mathrm{MSD}(\tau) = 6D_a\tau$. Because of the dispersion of the MSD curves (see Supporting information), the apparent diffusion coefficient D_a is averaged on numerous trajectories to minimize statistical error. At least 18 trajectories are used for each system.

In reality, diffusion within each clay mineral particle occurs in slit-shaped interlayer nanopores: In the present model, the layered internal microstructure of the particles can be accounted for by dividing each platelet into 20 sub-platelets of height ΔL. However, this model refinement considerably increases computational time. A series of simulations were performed with several configurations in which the platelets were subdivided by N (with N from 1 to 9). Each sub-platelet is then N-times thinner than the original ones. As a consequence, tracer displacement within each platelet is limited in the direction perpendicular to the basal surface. Hence the diffusion coefficients for different densities can be determined as a function of the number of subdivisions N (see Fig. 3). The diffusion coefficient noticeably decreases as N increases, especially for low densities where the platelets are thickest, until a plateau is reached at $N = 5$. Therefore, the simulations were performed with a sudivision of 5 to optimize the model while keeping the computational time as low as possible.

3.2. Input parameters

According to Eq. (9), the equilibrium concentration ratio between particles and interparticle pores (c_p/c_0) and the diffusion coefficients in the two phases (D_p and D_0) are required, for each species of interest, as input parameters of the simulations.

3.2.1. Concentrations

In the case of water and other inert tracers, equilibrium concentration in the interlayer is the same as in the interparticle pores. Therefore, c_p is related to c_0 through x_{il}:

$$c_p = c_0 \times x_{il}, \tag{10}$$

where x_{il} depends on ΔL (see Eq. (3)): c_p is smaller than c_0 because a part of the platelet is occupied by the solid. The model of ΔL as a function of ρ_b described in Section 2.1 directly yields c_p at each ρ_b. In the

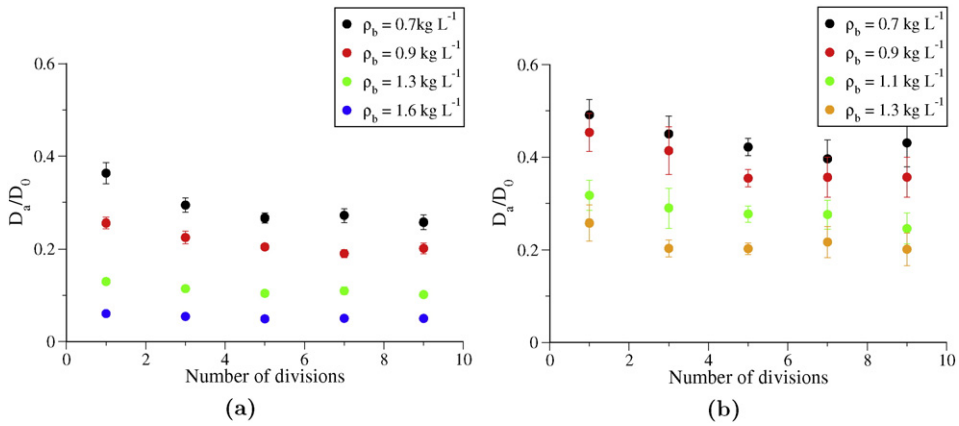

Fig. 3. Diffusion coefficients of uncharged tracers as a function of the number N of divisions in the platelets for densities ranging from 0.7 kg L^{-1} to 1.6 kg L^{-1} for (a) 'random' configurations and (b) Gay–Berne configurations.

case of ionic species, however, the equilibrium concentration ratio in the fluid inside and outside the interlayer pore, c_{int}/c_0, is not a priori equal to one. Because the clay mineral layers are negatively charged, there is an excess concentration of cations in the interlayer pores, while anions are partially excluded from them. In the model presented here, the Poisson-Boltzmann equation and the equality of chemical potentials in the interlayer and interparticle pores (Dufrêche et al., 2001; Hedström and Karnland, 2012) are used to numerically calculate the ratio c_{int}/c_0 as a function of c_0 for each hydration state of the interlayer pore (1W, 2W, 3W) (see Supporting information for more details). Then, as for water tracers, the global concentration in platelets where all interlayer pores are in the nW state can be obtained using the volumetric fraction of fluid x_{il}^{nW}: $c_p^{nW} = c_{int}^{nW} \times x_{il}^{nW}$. Thus, in a mixture of two types of pores (nW and mW) corresponding, for example, to 2W and 3W hydration states, the concentration inside the platelet becomes:

$$c_p = \frac{c_p^{nW} \times x_{nW}\left(\Delta L_{nW} - \Delta L_{dry}\right) + c_p^{mW} \times x_{mW}\left(\Delta L_{mW} - \Delta L_{dry}\right)}{\Delta L} \quad (11)$$

For clays in a natural environment, the ionic strength of the surrounding solution is of the order of 10^{-1} M. This value is used as an upper bound for the concentrations c_0 used for ions as tracers. The values of c_p at different ρ_b and ionic strength are given in Supporting information.

In the above equation, no change in ΔL was considered when the salinity varied, for lack of data. This assumption is somewhat questionable at small ρ_b values where the pores at 40 Å can partially coagulate in the presence of salt. However, in the case of a monovalent salt, the coagulation remains limited at small ionic strength (Michot et al., 2013). The ratio c_p/c_0 is higher than 1 for Na^+ and is very high at low ionic strength because the cations compensate the negative charge of the clay mineral layers. The ratio c_p/c_0 is smaller than 1 for Cl^- and is very low at low ionic strength because the anions are strongly excluded from the interlayer pores.

3.2.2. Diffusion coefficients

The diffusion coefficients of water and sodium in interlayer pores at different hydration states are available in the literature based on experimental and numerical simulation methods such as quasi-elastic neutron scattering (QENS) and molecular dynamics (MD) simulations.

In this work, diffusion coefficients of water in 1W- and 2W-interlayer pores were evaluated from QENS experiments (Malikova et al., 2006; Michot et al., 2007, 2012; Marry et al., 2013). The diffusion coefficients in 1W and 2W-interlayer pores are approximately ten and five times lower than in bulk water. The latter was estimated experimentally at 0.24 $Å^2$ ps^{-1} (Holz et al., 2000). Here, approximate diffusion coefficients based on these trends were used. They are summarized in Table 1. In the case of Na^+, diffusion coefficients were taken from previous MD simulations of Na^+ Mt with the CLAYFF force field (Bourg and Sposito, 2010). For water in 3W-interlayer pores and anions in 2W and 3W-interlayer pores, molecular dynamics simulations were carried out as part of the present study. The MD simulations used the LAMMPS code (Plimpton, 1995). The simulation box contained two clay mineral layers consisting of 32 unit cells of formula $Na_{0.75}Si_8(Al_{3.25}Mg_{0.75})O_{20}(OH)_4$. Interatomic interactions were described using the CLAYFF force field for montmorillonite (Cygan et al., 2004), the SPC/E model for water (Berendsen et al., 1987) and the Koneshan parameters for ions (Koneshan et al., 1998) derived from the work of Smith and Dang (1994). In order to evaluate Cl^- diffusion coefficients, 2 NaCl pairs were inserted in each interlayer pore and the number of water molecules was adjusted to reproduce the experimental ΔL values, i.e., 15.5 Å and 18.5 Å in the bi- and trihydrated state, which resulted in 12 or 18.9 water molecules per counter-ion, respectively. Trajectories were generated from four NVT simulations of 5 ns. Diffusion coefficients were calculated from the slope of the mean-squared displacement of Cl^- along the clay mineral layers between 100 and 500 ps (Frenkel and Smit, 1996). For interparticle pores and interlayer pores with $\Delta L \geq 40$ Å, the bulk diffusion coefficient was used (see Table 1).

In summary, one can note in Table 1 that all the species (water and ions) in 2W-interlayer pores are slowed down by a factor of 5–6 compared to their dynamics in bulk liquid water. In 3W-interlayer pores, the factor is 2 for water and about 3 for the ions.

For a mixture of two types of interlayer pores in a platelet, one can determine the volume-weighted average diffusion coefficient using

Table 1
Diffusion coefficients (in $Å^2$ ps^{-1}) of water, Na^+ and Cl^- in different kinds of interlayer (IL) and interparticle (IP) pores. The values for water were estimated based on QENS experiments (Malikova et al., 2006; Michot et al., 2007, 2012; Marry et al., 2013) and numerical simulations from the literature (Bourg and Sposito, 2010) and this work. Values for Na^+ were obtained from previously reported MD simulations (Bourg and Sposito, 2010). Values for Cl^- were obtained from MD simulations performed as part of the present study (values in italics). The D_0 values of all species (used to describe diffusion in the interparticle pores and, also, in interlayer nanopores with $\Delta L \geq 40$ Å) were taken from literature Bourg and Sposito (2010); Holz et al. (2000); Li and Gregory (1974); Koneshan et al. (1998).

Pore	Water	Na^+	Cl^-
1W-IL	*0.024*		
2W-IL	*0.048*	0.023[a]	*0.034*
3W-IL	*0.12*	0.042[a]	*0.055*
>3W-IL and IP	0.24[b]	0.133[a,c]	0.177[d]

[a] Bourg and Sposito (2010).
[b] Holz et al. (2000).
[c] Li and Gregory (1974).
[d] Koneshan et al. (1998).

Fick's law of diffusion, which gives:

$$D_p = \frac{x_{nW}\left(\Delta L_{nW} - \Delta L_{dry}\right) \times D_{nW} + x_{mW}\left(\Delta L_{mW} - \Delta L_{dry}\right) \times D_{mW}}{x_{nW}\left(\Delta L_{nW} - \Delta L_{dry}\right) + x_{mW}\left(\Delta L_{mW} - \Delta L_{dry}\right)} \quad (12)$$

for a mixture of *nW* and *mW* interlayer pores. See the Supporting information for more details.

4. Experimental database

Diffusion of dilute solutes in porous media can be described using an effective diffusion coefficient D_e ($m^2 s^{-1}$) or an apparent diffusion coefficient D_a. They are related by a factor α called the *rock capacity factor*:

$$D_e = \alpha D_a$$

where α is the equilibrium ratio between the total concentration of the species of interest per volume of porous medium (C_t) and the concentration of the 'free' species in the bulk-liquid-like pore fluid (C_b). When no adsorption occurs, $\alpha = \phi$ is the porosity and D_a only depends on the diffusion of the tracer in the pores and the geometry of the sample (Bourg and Tournassat, 2015).

Different experimental methods can be used to measure D_e and D_a. In *closed-cell* (CC) experiments (Sato et al., 1992; Kozaki et al., 1996b; Nakazawa et al., 1999; Tachi and Yotsuji, 2014), blocks of compacted, water-saturated bentonite are placed on both sides of a thin sample of tracer-enriched bentonite in a closed diffusion cell. After a time *t*, the bentonite is divided into slices to determine the new concentration profile, which yields D_a through Eq. (7). In the *through-diffusion* (TD) method (Muurinen et al., 1988; Choi and Oscarson, 1996; Van Loon et al., 2007; Gonzalez Sanchez et al., 2008; Glaus et al., 2013), a diffusion cell containing the porous medium is placed between two bulk water reservoirs, one of which is enriched with the tracer. The flux of the tracer reaching the tracer-depleted reservoir is monitored as a function of time and interpreted to obtain D_e and D_a. In *in-diffusion* (ID) experiments (Garcia-Gutierrez et al., 2004), the porous medium is in contact with a single reservoir doped with the tracer. One can determine both D_e and D_a by recording the decrease of the concentration in the source reservoir as a function of time and the concentration profile in the porous medium at the end of the experiment. Alternative methodologies for measuring diffusion coefficients exist such as electromigration experiments (Tanaka et al., 2011) and pulsed gradient spin echo ^{1}H nuclear magnetic resonance (PGSE ^{1}H NMR) (Nakashima, 2001, 2003a, 2003b, 2004; Nakashima and Mitsumori, 2005).

Experimental data on the diffusion coefficients of water, Na^+, and Cl^- (or I^-) at 298 K were taken from a recent compilation (Bourg and Tournassat, 2015). Confidence intervals ($\pm$95%) were calculated as $(B + 2V/n^{1/2}) \times D_a$, where *B* quantifies systematic errors as a fraction of D_a, *V* is the coefficient of variation associated with random errors, and *n* is the number of replicates. The value of *V* was taken from Bourg et al. (2006) ($V = 0.11$) and *B* was roughly estimated to 0.2 for most experimental results. However, for TD and ID studies that did not account for the impact of filter-plates on their diffusion results, the latter was increased to $B = 0.5$ in order to reflect the expected lower accuracy of these studies.

5. Results and discussion

5.1. Porous medium

Several trajectories were simulated for different configurations of the clay platelets. Overall, diffusion coefficients obtained for configurations generated from Gay–Berne potentials (designated as 'GB' configurations) are 1.6 to 2.1 times greater than for 'random' configurations, for every kind of tracer. This can be explained by the lower tortuosity of those configurations. Indeed, tortuosity is the ratio of the average length of the fluid path between two points of a porous medium and the geometrical distance between those points. Large regions where platelets are organized according to a preferential orientation exist in GB configurations (see Fig. 1), which creates straight paths and should result in a lower tortuosity relative to the completely random configurations. Besides, due to the way they are generated, the diffusion is slightly anisotropic for GB configurations: The diffusion coefficients along the *x*-, *y*- and *z*-axis are not equivalent (i.e., $D_x^{GB} \neq D_y^{GB} \neq D_z^{GB}$). For random isotropic configurations, however, they are similar. This is merely an artifact from the MD simulations: Because the simulation box is not infinite, the arrangement of the GB ellipsoids cannot be fully isotropic, as it should be with an infinite box since no direction is favored by pressure in the MD simulations. The fact remains that, because of the uniaxial sample compression, the compacted bentonite used in diffusion experiments is indeed not isotropic and therefore the experimental diffusion tensor displays asymmetry (Bourg and Tournassat, 2015). However, given the nature of the MD simulations performed here, this aspect of the diffusion will not be further investigated and only he average D_a value in all three directions will be discussed from now on.

In order to gain further insight into the influence of particle arrangements on pore network geometry, the number and the size of the interparticle pores were investigated in both GB and 'random' configurations at $\rho_b = 1.3$ kg L^{-1}. For that purpose, tracers were only allowed to diffuse in interparticle pores. The zones explored by the tracer were found to be less numerous but much larger for Gay–Berne configurations than for 'random' ones, which show less connectivity between the interparticle pores. At $\rho_b = 1.3$ kg L^{-1}, the average volume of connected interparticle pores is more than three times higher for the GB configuration ($\sim 2.3 \times 10^8$ Å^3) than for the 'random' one ($\sim 7.1 \times 10^7$ Å^3). The largest connected interparticle pores for both configurations are displayed in Fig. 4 for illustrative purposes. The higher connectivity found for GB configurations is consistent with the ratio D_a/D_0 being higher for these configurations than for 'random' ones, as will be shown below.

Furthermore, because of the way the porous medium is created, small portions of particles or pores may be inaccessible to the tracer (e.g., volumes delimited only by basal surfaces of platelets). As a consequence, the ratio between the volume of platelets explored by the tracer and the total volume explored by the tracer can differ from the theoretical φ used to generate the porous sample (cf. Section 2). These unconnected zones were located by exploring the simulation boxes and detecting regions where the tracers were confined. The volume of these zones in 'random' configurations was found to represent between 0.6% to 1% of the total volume of the simulation box while in GB configurations they represented 0.015% of the total volume at most. In fact, GB configurations had very few lost volumes or even no lost volume at all for densities inferior to 1.3 kg L^{-1}. The much smaller number of such zones for GB configurations than for random ones is consistent with the fact that GB configurations display a better connectivity than 'random' configurations. In both cases, the accessible porosity was found to differ from the theoretical φ by at most 0.6%.

5.2. Diffusion

Diffusion coefficients calculated from Brownian dynamics simulations of water tracers in 'random' and GB configurations are compared with experimental D_a values in Fig. 5. Measured and predicted diffusion coefficients values are not entirely equivalent, in that the former were obtained with samples anisotropically compacted in the same direction as the diffusion measurement, whereas the latter were obtained with essentially isotropic systems. The difference is negligible at $\rho_b < 0.8$ kg L^{-1} and amounts to a factor of ~1.5 to 3 at $\rho_b = 1.5$ kg L^{-1} (Bourg and Tournassat, 2015).

Despite the significant scatter in the experimental results, the simulations clearly capture the essential features of the real system. In particular, the ρ_b-dependence of the diffusion coefficient is broadly consistent with the measured trend. Overall, predictions obtained with the GB

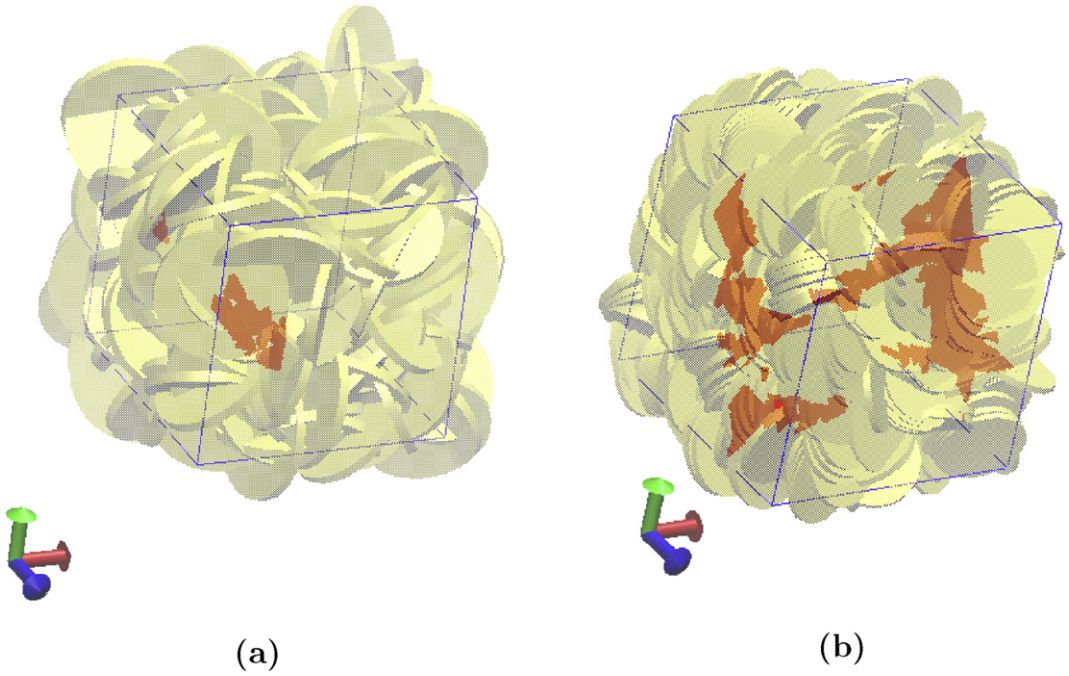

Fig. 4. Visualization of the largest connected interparticle pores (in dark red) for a sample of density $\rho b = 1.3$ kg L^{-1} with (a) a 'random' configuration of platelets and (b) a Gay–Berne configuration of platelets.

configuration consistently overestimate the best available experimental data (black symbols) by a factor of ~2 to 4.

Closer examination of the simulation predictions with the GB configuration reveals that the decrease in D_a/D_0 between $\rho_b = 0.7$ kg L^{-1} and 1.6 kg L^{-1} by a factor of 4.6 can be primarily attributed to the reduction of D_p/D_0 by a factor 3.4 (cf Supporting information) and also, to a much smaller extent, to a change in porous geometry with increasing ρ_b (larger tortuosity, smaller connectivity between interparticle pores, smaller interparticle pore size).

Experimental data on the diffusion of Cl^- and Na^+ are compiled and displayed in Figs. 6 and 7, respectively, along with BD simulation predictions. For both types of species, several ionic strengths were investigated (from 0.001 M to 0.1 M). In the case of anions, for the densities corresponding to mixtures of 2W- and 3W-layers, two configurations were explored with 84% and 21% of 3W-layers, respectively ($\rho_b =$ 1.4 kg L^{-1} and $\rho_b = 1.6$ kg L^{-1}). Although enough trajectories were simulated to obtain the diffusion coefficient for an ionic strength of 0.1 M for both densities, simulations were inconclusive for lower ionic strengths for $\rho_b = 1.6$ kg L^{-1} where most interlayer spaces are 2W hydrates. Indeed, in most of the trajectories, the tracer remains in small regions of the simulation box because of the low value of the ratio c_p/c_0. An accurate estimation of D_a would require much longer simulations.

For every ionic strength, results from simulations for Cl^- are in good agreement with experimental data on D_a/D_0, especially for GB configurations. In the case of random configurations, the poor connectivity between interparticle pores forces anions to diffuse through the platelets. This is strongly inhibited at high ρ_b and low ionic strength, because of the very low value of c_p/c_0 (see Fig. 6b).

The agreement between simulations and experiments is recovered when anion diffusion results are expressed as $(D_a/D_0)_{Cl^-}/(D_a/D_0)_{water}$ as shown in in Fig. 6c. The decrease of this ratio when increasing ρ_b derives from the stronger decrease of c_p/c_0 with ρ_b for Cl^- than for H_2O,

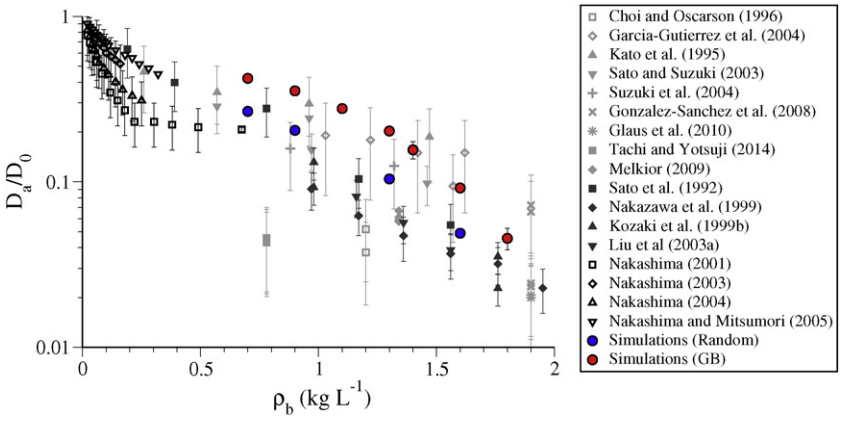

Fig. 5. Diffusion coefficient of water obtained by Brownian dynamics simulations with GB and random configurations consisting of platelets divided in 5 (in red and blue, respectively) as a function of ρ_b compared with experimental data for water diffusion in bentonite. Black symbols are used for the best available data obtained by standard measurement techniques such as TD or CC (Sato et al., 1992; Kozaki et al., 1999b; Nakazawa et al., 1999; Liu et al., 2003a) (full symbols) or by NMR (Nakashima, 2001, 2003a, 2003b, 2004; Nakashima and Mitsumori, 2005) (open symbols); data obtained without account for the influence of filter-plates (Choi and Oscarson, 1996; Garcia-Gutierrez et al., 2004) and with no sampling of concentration profiles in the clay (Kato et al., 1994; Sato and Suzuki, 2003; Suzuki et al., 2004; Gonzalez Sanchez et al., 2008; Melkior et al., 2009; Glaus et al., 2010; Tachi and Yotsuji, 2014) are shown in open and full gray symbols, respectively.

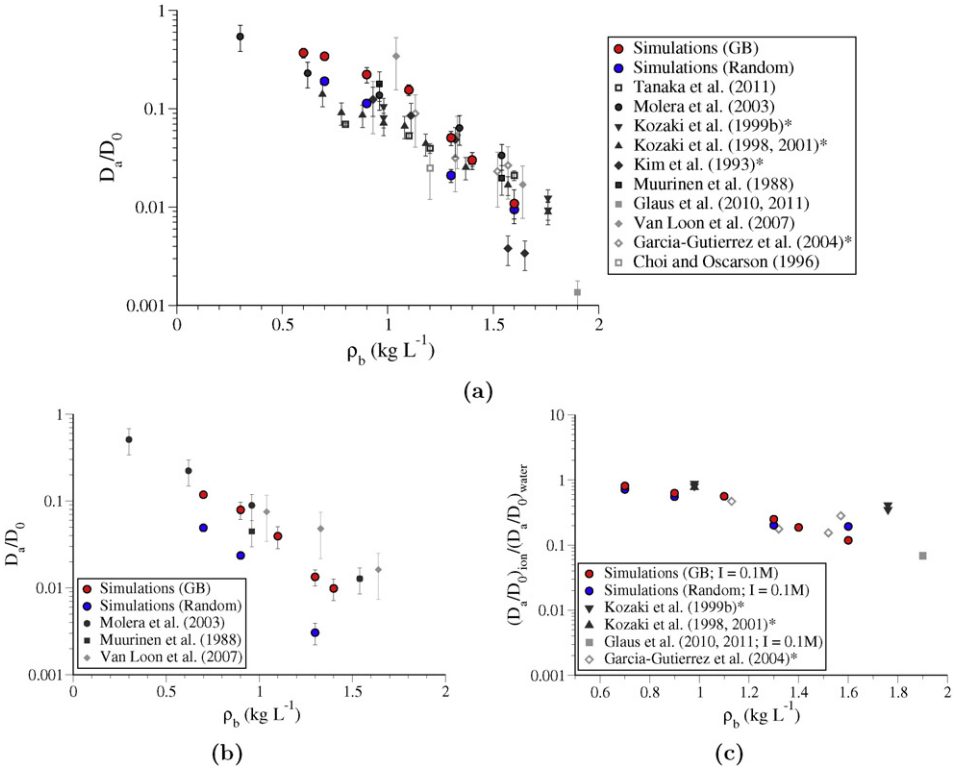

Fig. 6. Same as in Fig. 5 in the case of Cl^- at two ionic strengths in panels (a) $I = 0.1$ *M* and (b) $I = 0.01$ M. Panel (c) shows predicted and experimental data on the ratio $(D_a/D_0)Cl^-/(D_a/D_0)$water as a function of ρ_b. The star indicates when the clay is saturated with pure water. Black symbols are used for the best available data obtained by standard measurement techniques such as TD or CC (Muurinen et al., 1988; Kim et al., 1993; Kozaki et al., 1998b, 1999b, 2001a; Molera et al., 2003) (full symbols) or by electromigration experiments (Tanaka et al., 2011) (open symbols); data obtained without account for the influence of filter-plates (Choi and Oscarson, 1996; Garcia-Gutierrez et al., 2004) and with no sampling of concentration profiles in the clay (Van Loon et al., 2007; Glaus et al., 2010, 2011) are shown in open and full gray symbols, respectively.

which is a direct consequence of anion exclusion. The inflection observed on the simulated curve near $\rho_b = 1.3$ kg L^{-1} coincides with the inflection of c_p/c_0 as a function of ρ_b (see Supporting information), which approximately corresponds to the transition from a mixture of 3W and 40 Å states to a mixture of 3W and 2W hydration states.

Predicted anion diffusion coefficients clearly display a strong salinity dependence (see Fig. 8a), in agreement with most of the experimental data which show a global increase in D_a/D_0 with I. The simulations show that this increase is caused by the increase in c_p/c_0 with increasing ionic strength. This means that anions do not solely travel in the interparticle pore space, where the salinity should have no influence in the present model, and that diffusion through the platelets significantly impacts the overall diffusive flux: Anions spend most of their time in interparticle pores, but they sometimes must travel through the platelets in order to diffuse from an interparticle pore to another, and this transition is highly sensitive to salinity. This finding is further supported by the results for random configurations (not shown), where the salinity dependence is stronger and increases more strongly with ρ_b than in GB configurations, because the smaller interparticle pores and lower connectivity of the random system force anionic tracers to pass through more particles in order to diffuse through the porous medium.

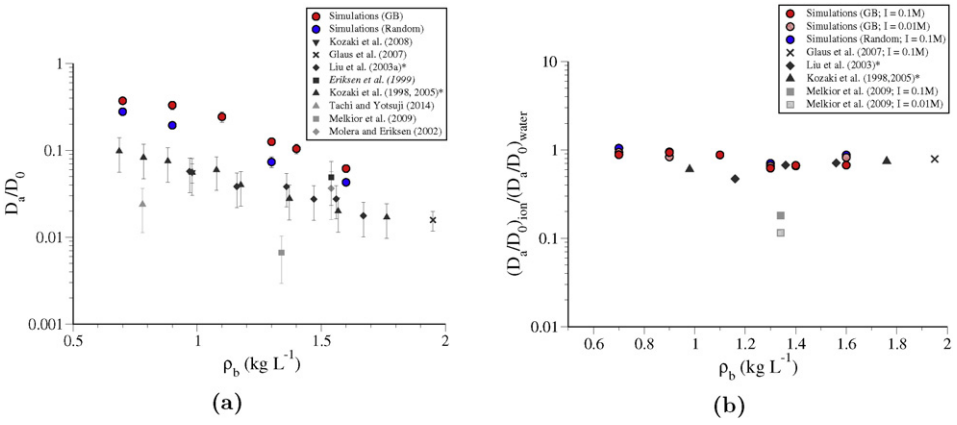

Fig. 7. Same as in Fig. 6 in the case of Na^+: (a) D_a/D_0 as a function of ρ_b in bentonite at $I = 0.1$ *M*; (b) $(D_a/D_0)_{Na+}/(D_a/D_0)_{water}$ as a function of ρ_b. The star indicates when the clay was saturated with pure water, the italics indicates that the ionic strength is unknown. Black symbols are used for the best available data obtained by standard measurement techniques such as TD or CC (Kozaki et al., 1998a, 2005, 2008; Eriksen et al., 1999; Liu et al., 2003a; Glaus et al., 2007); data obtained with no sampling of concentration profiles in the clay (Molera and Eriksen, 2002; Melkior et al., 2009; Tachi and Yotsuji, 2014) are shown in gray symbols.

Experimental data and simulations results on D_a/D_0 for Na^+ in bentonite are shown in Fig. 7a. While both experiments and simulations show a fairly similar dependence on ρ_b, as also reported in the case of water and Cl^-, the diffusion coefficients from the simulations are up to three times larger than the experimental ones. The ratio $(D_a/D_0)_{Na^+}/(D_a/D_0)_{water}$ is between 0.5 and 1 for all dry densities, in good agreement with most of the experimental results. This is consistent with the fact that for these experiments (Liu et al., 2003a) and Kozaki et al. (1998a, 2005), simulations also overestimate the water diffusion coefficients (Fig. 5).

Because of their large c_p/c_0 ratio, cations are expected to diffuse primarily via the platelets and the interparticle pores should have little influence on D_a/D_0. Therefore, the fact that the simulations overestimate D_a/D_0 may result from a too high connectivity between the platelets. In the simulations, a tracer goes from one platelet to another with a probability of one, as long as it does not cross a basal surface. As a consequence, cationic tracers can diffuse through a large part of the sample without passing through interparticle pores. The good connectivity of the platelets in the simulations is evidenced by the fact that, contrary to the Cl^- case, salinity has little impact on the D_a/D_0 values of Na^+: Fig. 8b illustrates that the variation of D_a/D_0 as a function of I remains small compared to the anion case, in good agreement with the experimental database.

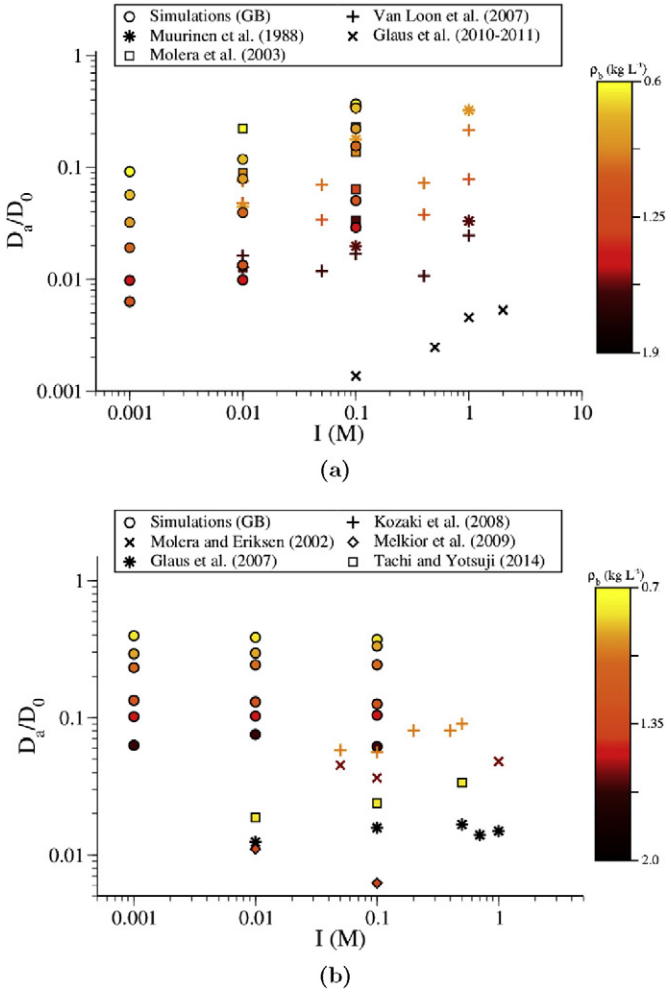

Fig. 8. Ratio of the diffusion coefficients D_a/D_0 as a function of the ionic strength I for various densities (from low densities in yellow to high densities in black): (a) comparison between simulations results and experimental data (Muurinen et al., 1988; Molera et al., 2003; Van Loon et al., 2007; Glaus et al., 2010, 2011) for Cl^-; (b) comparison between simulations results and experimental data (Molera and Eriksen, 2002; Glaus et al., 2007; Kozaki et al., 2008; Melkior et al., 2009; Tachi and Yotsuji, 2014) for Na^+.

The 'asymmetry' between cation and anion diffusion noted above (minor salinity-dependance of D_a for the former, large salinity-dependance for the latter) is further expressed by the fact that the diffusion coefficients obtained with 'random' configurations are up to 4.4 times smaller than the ones calculated from trajectories in GB configurations in the case of Cl^-, but only 1.3 to 1.8 times smaller in the case of Na^+. As noted above, the main difference between the two types of configurations is that GB configurations display a better connectivity between interparticle pores. This connectivity strongly facilitates the diffusion of the anions while having relatively little impact on the diffusion of cations (which diffuse mostly within the particles). These observations are consistent with the results of less coarse-grained simulations that account explicitly for electrostatic effects, in particular the 'electrostatic bottlenecks' experienced by anions as they diffuse between interparticle pores (Rotenberg et al., 2010; Jardat et al., 2012).

One possible improvement to this model would consist in decreasing the probability to go from one platelet to another. Such a change would decrease the connectivity between platelets, which would decrease the D_a/D_0 values of cations (and, to a smaller extent, of water) while having little impact on the D_a/D_0 values of anions, potentially bringing all GB simulation predictions in closer agreement with the experimental database.

6. Conclusion

A Brownian dynamics simulation methodology was developed to investigate the diffusion of cationic (Na^+), anionic (Cl^-), and water tracers in compacted, water-saturated montmorillonite, on scales of micrometers and milliseconds. A new model of clay mineral particles is introduced in which cylindrical platelets can overlap, which allows to represent highly compacted samples. Diffusion in individual pores (interlayer nanopores and interparticle mesopores) was modeled using two different diffusion coefficients determined from experimental and simulation results obtained at nanometer and nanosecond scales.

Overall, the simulations broadly predict the major features of water, Na^+, and Cl^- diffusion in compacted clays as a function of density and ionic strength. The main discrepancy with the experimental database is that the model overestimates the D_a values of Na^+ (by a factor of ~4) and of water (by a factor of ~2). This can be ascribed, at least in part, to the simplicity of the structure used to model the clay. One way of improving the existing model would be to refine the effect of the sample structure on the diffusion behavior of the tracer by tuning the transition probability between particles. Such a modification would decrease the D_a values of Na^+ and, to a lesser extent, of water tracers and improve the agreement with experimental results. Another way of improving the model would be to take into account the effect of compaction along one direction, which was neglected in this work. For example, new porous media could be generated by applying a higher pressure in one direction on the system constituted by ellipsoidal particles (see Section 2.2). The connectivity between interparticle pores should, then, be higher and the tortuosity lower in the direction perpendicular to the compaction, with consequences regarding the asymmetry of the diffusion tensor, as observed experimentally in anisotropically-compacted clays and clay-rocks.

Acknowledgements

The authors thank Roland Pellenq and Davoud Ebrahimi for helpful discussions and for providing us configurations of ellipsoidal platelets from which the GB configurations are derived.

The DOE Office of Science, Office of Basic Energy Sciences supported I. C. Bourg under Contract DE-AC02-05CH11231.

Appendix A. Supporting information

Supplementary data to this article can be found online at http://dx.doi.org/10.1016/j.clay.2015.12.014.

References

ANDRA report, 2001. Référentiel matériaux, tome 2: Les matériaux argileux. Technical report. ANDRA.

Arnott, R.J., 1965. Particle sizes of clay minerals by small-angle X-ray scattering. Am. Mineral. 50, 1563–1575.

Berendsen, H.J.C., Grigera, J.R., Straatsma, T.P., 1987. The missing term in effective pair potentials. J. Phys. Chem. 91 (24), 6269–6271.

Birgersson, M., Karnland, O., 2009. Ion equilibrium between montmorillonite interlayer space and an external solution — consequences for diffusional transport. Geochim. Cosmochim. Acta 73, 1908–1923.

Bourg, I.C., Sposito, G., 2010. Connecting the molecular scale to the continuum scale for diffusion processes in smectite-rich porous media. Environ. Sci. Technol. 44 (6), 2085–2091.

Bourg, I.C., Tournassat, C., 2015. Self-diffusion of water and ions in clay barriers. In: Tournassat, C., Steefel, C.I., Bourg, I.C., Bergaya, F. (Eds.), Natural and Engineered Clay Barriers, first ed. Developments in Clay Science vol. 6, chapter 6. Elsevier.

Bourg, I.C., Sposito, G., Bourg, A.C.M., 2006. Tracer diffusion in compacted, water-saturated bentonite. Clay Clay Miner. 54 (3), 363–374.

Calvet, R., 1973. Hydratation de la montmorillonite et diffusion des cations compensateurs. Ann. agron. 24, 77–217.

Cases, J.M., Bérend, I., Besson, G., François, M., Uriot, J.P., Thomas, F., Poirier, J.E., 1992. Mechanism of adsorption and desorption of water vapor by homoionic montmorillonite. 1. The sodium-exchanged form. Langmuir 8, 2730–2739.

Choi, J.W., Oscarson, D.W., 1996. Diffusive transport through compacted Na- and Ca-bentonite. J. Contam. Hydrol. 22, 189–202.

Churakov, S.V., Gimmi, T., 2011. Up-scaling of molecular diffusion coefficients in clays: A two-step approach. J. Phys. Chem. C 115, 6703–6714.

Churakov, S.V., Gimmi, T., Unruh, T., Van Loon, L.R., Juranyi, F., 2014. Resolving diffusion in clay minerals at different time scales: Combination of experimental and modeling approaches. ACS 96, 36–44.

Coelho, D., Thovert, J.F., Adler, P.M., 1997. Geometrical and transport properties of random packings of spheres and asperical particles. Phys. Rev. E 55 (2), 1959–1978.

Crank, J., 1975. The Mathematics of Diffusion. second ed. Clarendon Press, Oxford.

Cygan, R.T., Liang, J.J., Kalinichev, A.G., 2004. Molecular models of hydroxide, oxyhydroxyde, and clay phases and the development of a general force field. J. Phys. Chem. B 108 (4), 1255–1266.

Delville, A., 1992. Structure of liquids at a solid interface: An application to the swelling of clay by water. Langmuir 8, 1796–1805.

Dufrêche, J.F., Marry, V., Bernard, O., Turq, P., 2001. Models for electrokinetic phenomena in montmorillonite. Colloids Surf. A Physicochem. Eng. Asp. 195, 171–180.

Ebrahimi, D., Whittle, A.J., Pellenq, R.J.M., 2014. Mesoscale properties of clay aggregates from potential of mean force representation of interactions between nanoplatelets. J. Chem. Phys. 140 (154309), 1–17.

Eriksen, T.E., Jansson, M., Molera, M., 1999. Sorption effects on cation diffusion in compacted bentonite. Eng. Geol. 54, 231–236.

Ferrage, E., Lanson, B., Sakharov, B.A., Drits, V.A., 2005b. Investigation of smectite hydratation properties by modeling experimental X-ray diffraction patterns: part I. Montmorillonite hydration properties. Am. Mineral. 90 (8–9), 1358–1374.

Frenkel, D., Smit, B., 1996. Understanding Molecular Simulation: from Algorithms to Applications. Academic Press, San Diego.

Fu, M.H., Zhang, Z.Z., Low, P.F., 1990. Changes in the properties of a montmorillonite-water system during the adsorption and desorption of water: hysteresis. Clay Clay Miner. 38, 485–492.

Garcia-Gutierrez, M., Cormenzana, J.L., Missana, T., Mingarro, M., 2004. Diffusion coefficients and accessible porosity for HTO and ^{36}Cl in compacted FEBEX bentonite. Appl. Clay Sci. 26, 65–73.

Glaus, M.A., Baeyens, B., Bradbury, M.H., Jakob, A., Van Loon, L.R., Yaroshchuk, A., 2007. Diffusion of ^{22}Na and ^{85}Sr in montmorillonite: evidence of interlayer diffusion being the dominant pathway at high compaction. Environ. Sci. Technol. 41, 478–485.

Glaus, M.A., Birgersson, M., Karnland, O., Van Loon, L.R., 2013. Seeming steady-state uphill diffusion of $^{22}Na^+$ in compacted montmorillonite. Environ. Sci. Technol. 47, 11522–11527.

Glaus, M.A., Frick, S., Rossé, R., Van Loon, L.R., 2010. Comparative study of tracer diffusion of HTO, $^{22}Na^+$ and $^{36}Cl^-$ in compacted kaolinite, illite and montmorillonite. Geochim. Cosmochim. Acta 74, 1999–2010.

Glaus, M.A., Frick, S., Rossé, R., Van Loon, L.R., 2011. Consistent interpretation of the results of through-, out-diffusion and tracer profile analysis for trace diffusion in compacted montmorillonite out-diffusion and tracer profile analysis for trace diffusion in compacted montmorillonite. J. Contam. Hydrol. 123, 1–10.

Gonzalez Sanchez, F., Van Loon, L.R., Gimmi, T., Jakob, A., Glaus, M.A., Diamond, L.W., 2008. Self-diffusion of water and its dependence on temperature and ionic strength in highly compacted montmorillonite, illite and kaolinite. Appl. Geochem. 23, 3840–3851.

H12 report, 2000. H12 report: project to establish the scientific and technical basis for HLW disposal in Japan. Supporting Report 3: Safety Assessment of the Geological Disposal SystemTechnical Report. Japan Nuclear Cycle Development Institute.

Hedström, M., Karnland, O., 2012. Donnan equilibrium in Na-montmorillonite from a molecular dynamics perspective. Geochim. Cosmochim. Acta 77, 266–274.

Holmboe, M., Wold, S., Jonsson, M., 2012. Porosity investigation of compacted bentonite using XRD profile modeling. J. Contam. Hydrol. 128, 19–32.

Holz, M., Heil, S.R., Sacco, A., 2000. Temperature-dependent self-diffusion coefficients of water and six selected molecular liquids for calibration in accurate ^1H NMR PFG measurements. Phys. Chem. Chem. Phys. 2, 4740–4742.

Hueckel, T., Loret, B., Gajo, A., 2002. Expansive clays as two-phase, deformable reactive continua: concepts and modeling options. In: Di Maio, C., Hueckel, T., Loret, B. (Eds.), Chemo-Mechanical Coupling in Clays. Balkema Publishers, pp. 105–120.

Jardat, M., Dufrêche, J.F., Marry, V., Rotenberg, B., Turq, P., 2009. Salt exclusion in charged porous media: a coarse-graining strategy in the case of montmorillonite clays. Phys. Chem. Chem. Phys. 11, 2023–2033.

Jardat, M., Hribar-Lee, B., Vlachy, V., 2012. Self-diffusion of ions in charged nanoporous media. Soft Matter 8, 954–964.

Karnland, O., Olsson, S., Nilsson, U., 2006. Mineralogy and sealing properties of various bentonites and smectite-rich clay materials. Technical Report. Swedish Nuclear Fuel and Waste Management Co., SKB AB.

Kato, H., Muroi, M., Yamada, N., Ishida, H., Sato, H., 1994. Estimation of effective diffusivity in compacted ben tonite. Symposium — Scientific Basis for Nuclear Waste Management XVIII, MRS Proceedings, Volume 353.

Kim, H., Suk, T., Park, S., Lee, C., 1993. Diffusivities for ions through compacted Na-bentonite with varying dry bulk density. Waste Manag. 13, 303–308.

Koneshan, S., Rasaiah, J.C., Lynden-Bell, R.M., Lee, S.H., 1998. Solvent structure, dynamics, and ion mobility in aqueous solutions at 25 °C. J. Phys. Chem. B 102, 4193–4204.

Kozaki, T., Sato, H., Fujishima, A., Saito, N., Sato, S., Ohashi, H., 1996a. Effect of dry density on activation energy for diffusion of strontium in compacted sodium montmorillonite. Symposium II — Scienfific Basis for Nuclear Waste Management XX, MRS Proceedings, volume 465.

Kozaki, T., Sato, H., Fujishima, A., Sato, S., Ohashi, H., 1996b. Activation energy for diffusion of cesium in compacted sodium montmorillonite. J. Nucl. Sci. Technol. 33 (6), 522–524.

Kozaki, T., Fujishima, A., Saito, N., Sato, S., Ohashi, H., 2005. Effects of dry density and exchangeable cations on the diffusion process of sodium ions in compacted montmorillonite. Eng. Geol. 81, 246–254.

Kozaki, T., Fujishima, A., Sato, S., Ohashi, H., 1998a. Self-diffusion of sodium ions in compacted sodium montmorillonite self-diffusion of sodium ions in compacted sodium montmorillonite self-diffusion of sodium ions in compacted sodium montmorillonite. Nucl. Technol. 121, 63–69.

Kozaki, T., Inada, K., Sato, S., Ohashi, H., 2001a. Diffusion mechanism of chloride ions in sodium montmorillonite. J. Contam. Hydrol. 47, 159–170.

Kozaki, T., Liu, J., Sato, S., 2008. Diffusion mechanism of sodium ions in compacted montmorillonite under different NaCl concentration. Phys. Chem. Earth 33, 957–961.

Kozaki, T., Saito, N., Fujishima, A., Sato, S., 1998b. Activation energy for diffusion of chloride ions in compacted sodium montmorillonite. J. Contam. Hydrol. 35, 67–75.

Kozaki, T., Sato, Y., Nakajima, M., Kato, H., Sato, S., Ohashi, H., 1999b. Effect of particle size on the diffusion behavior of some radionuclides in compacted bentonite. J. Nucl. Mater. 270, 265–272.

Leote de Carvalho, R.J.F., Skipper, N.T., 2001. Atomistic computer simulation of the clay-fluid interface in colloidal laponite. J. Chem. Phys. 114 (8), 3727–3733.

Li, Y.H., Gregory, S., 1974. Diffusion of ions in sea water and in deepsea sediments. Geochim. Cosmochim. Acta 38, 703–714.

Liu, J., Yamada, H., Kozaki, T., Sato, S., Ohashi, H., 2003a. Effect of silica sand on activation energy for diffusion of sodium ions in montmorillonite and silica sand mixture. J. Contam. Hydrol. 61, 85–93.

Malikova, N., Cadène, A., Marry, V., Dubois, E., Turq, P., 2006. Diffusion of water in clays on the microscopic scale: Modeling and experiment. J. Phys. Chem. B 110, 3206–3214.

Marry, V., Dubois, E., Malikova, N., Breu, J., Haussler, W., 2013. Anisotropy of water dynamics in clays: insights from molecular simulations for experimental qens analysis. J. Phys. Chem. C 117, 15106–15115.

McCombie, C., 1997. Nuclear waste management worldwide. Phys. Today 56–62.

Melkior, T., Gaucher, E.C., Brouard, C., Yahiaoui, S., Thoby, D., Clinard, C., Ferrage, E., Guyonnet, D., Tournassat, C., Coelho, D., 2009. Na^+ and HTO diffusion in compacted bentonite: effect of surface chemistry and related texture. J. Hydrol. 370, 9–20.

Michot, L.J., Bihannic, I., Thomas, F., Lartiges, B.S., Waldvogel, Y., Caillet, C., Thieme, J., Funari, S.S., Levitz, P., 2013. Coagulation of Na-montmorillonite by inorganic cations at neutral pH. A combined transmission X-ray microscopy, small angle and wide angle X-ray scattering study. Langmuir 29 (10), 3500–3510.

Michot, L.J., Delville, A., Humbert, B., Plazanet, M., Levitz, P., 2007. Diffusion of water in a synthetic clay with tetrahedral charges by combined neutron time-of-flight measurements and molecular dynamics simulations. J. Phys. Chem. C 111, 9818–9831.

Michot, L.J., Ferrage, E., Jiménez-Ruiz, M., Boehm, M., Delville, A., 2012. Anisotropic features of water and ion dynamics in synthetic Na- and Ca-smectites with tetrahedral layer charge. a combined quasi-elastic neutron-scattering and molecular dynamics simulations study. J. Phys. Chem. C 116, 16619–16633.

Molera, M., Eriksen, T.E., 2002. Diffusion of ^{22}Na, $^{85}Sr^{2+}$, $^{134}Cs^+$ and $^{57}Co^{2+}$ in bentonite clay compacted to different densities: experiments and modeling. Radiochim. Acta 90, 753–760.

Molera, M., Eriksen, T.E., Jansson, M., 2003. Anion diffusion pathways in bentonite clay compacted to different dry densities. Appl. Clay Sci. 23, 69–76.

Muurinen, A., Pemtilä-Hiltunen, P., Uusheimo, K., 1988. Diffusion of chloride and uranium in compacted sodium bentonite. Symposium BERLIN — Scientific Basis for Nuclear Waste Management XII, MRS Proceedings, volume 127.

Nakashima, Y., 2001. Pulsed field gradient NMR study of the self-diffusion of H_2O in montmorillonite gel: effects of temperature and water fraction. Am. Mineral. 85, 132–138.

Nakashima, Y., 2003a. Diffusion of H_2O in smectite gels: obstruction effects of bound H_2O layers. Clay Clay Miner. 51, 9–22.

Nakashima, Y., 2003b. Diffusivity measurement of heavy ions in Wyoming montmorillonite gels by X-ray computed tomography. J. Contam. Hydrol. 61, 147–156.

Nakashima, Y., 2004. Nuclear magnetic resonance properties of water-rich gels of Kunigel-V1 bentonite. J. Nucl. Sci. Technol. 41, 921–992.
Nakashima, Y., Mitsumori, F., 2005. H_2O self-diffusion restricted by clay platelets with immobilized bound H_2O layers: PGSE NMR study of water-rich saponite gels. Appl. Clay Sci. 28, 209–221.
Nakazawa, T., Takano, M., Nobuhara, A., Torikai, Y., Sato, S., Ohashi, H., 1999. Activation energies of diffusion of tritium and electrical conduction in water-saturated compacted sodium montmorillonite. Radioactive Waste Management and Environmental Remediation-ASME.
Norrish, K., 1954. The swelling of montmorillonite. Discuss. Faraday Soc. 18, 120–134.
Norrish, K., Quirk, J.P., 1954. Crystalline swelling of montmorillonite: Use of electrolytes to control swelling. Nature 173, 255–256.
Plimpton, S., 1995. Fast parallel algorithms for short-range molecular dynamics. J. Comput. Phys. 117, 1–19.
Rotenberg, B., Marry, V., Vuilleumier, R., Malikova, N., Simon, C., Turq, P., 2007. Water and ions in clays: unraveling the interlayer/micropore exchange using molecular dynamics. Geochim. Cosmochim. Acta 71, 5089–5101.
Rotenberg, B., Pagonabarraga, I., Frenkel, D., 2010. Coarse-grained simulations of charge, current and flow in heterogeneous media. Faraday Discuss. 144, 223–243.
Sato, H., Suzuki, S., 2003. Fundamental study on the effect of an orientation of clay particles on diffusion pathway in compacted bentonite. Appl. Clay Sci. 23, 51–60.
Sato, H., Ashida, T., Kohara, Y., Yui, M., Sasaki, N., 1992. Effect of dry density on diffusion of some radionuclides in compacted sodium bentonite. J. Nucl. Sci. Technol. 29, 873–882.
Skipper, N.T., Lock, P.A., Titiloye, J.O., Swenson, J., Mirza, Z.A., Howells, W.S., 2006. The structure and dynamics of 2-dimensional fluids in swelling clays. Chem. Geol. 230, 182–196.
Smith, D.E., Dang, L.X., 1994. Computer simulations of NaCl association in polarizable water. J. Chem. Phys. 100, 3757–3765.
Suzuki, S., Sato, H., Ishidera, T., Fujii, N., 2004. Study on anisotropy of effective diffusion coefficient and activation energy for deuterated water in compacted sodium bentonite. J. Contam. Hydrol. 68, 23–37.
Tachi, Y., Yotsuji, K., 2014. Diffusion and sorption of Cs^+, Na^+, I^- and HTO in compacted sodium montmorillonite as a function of porewater salinity: Integrated sorption and diffusion model. Geochim. Cosmochim. Acta 132, 75–93.
Tanaka, S., Noda, N., Sato, S., Kozaki, T., Sato, H., Hatanaka, K., 2011. Electrokinetic study of migration anions, cations, and water in water-saturated compacted sodium montmorillonite. J. Nucl. Sci. Technol. 48, 454–462.
Thovert, J.F., Yousefian, F., Spanne, P., Jacquin, C.G., Adler, P.M., 2001. Grain reconstruction of porous media: Application to a low-porosity Fontainebleau sandstone. Phys. Rev. Early 63 (061307).
Tyagi, M., Gimmi, T., Churakov, S.V., 2013. Multi-scale micro-structure generation strategy for up-scaling transport in clays. Adv. Water Resour. 59, 181–195.
Van Loon, L.R., Glaus, M.A., Müller, W., 2007. Anion exclusion effects in compacted bentonites: Towards a better understanding of anion diffusion. Appl. Geochem. 22, 2536–2552.